

Self-driven nanofluidics at liquid-gas interface

Vinitha Johny and Siddharth Ghosh^{†*}

Department of Science, Open Academic Research Council, Kolkata, India.

Department of Science, Open Academic Research UK CIC, Cambridge, UK.

International Centre for Nanodevices, Centre for Nano Science and Engineering, Indian Institute of Science, Bangalore.

[†]*Department of Applied Mathematics and Theoretical Physics, University of Cambridge, UK.*

We report a novel flow dynamics at the interface of liquid and gas through nanofluidic pores without applying any external driving force. Rayleigh-Taylor instability of water and air in sub-100 nanometer fluidic pores in a micrometre square domain of water and air are studied. We analyse it in the context of parameters, such as applied pressure, position to pore size ratio of the nanofluidic pore, gravity, and density. Our research also verifies the flow velocity equation with the simulation results and discuss the mass transfer efficiency of such flow structures. This is the first report on a self-driven switching mechanism of nanofluidic flow from ON to OFF or vice versa. A highly nonlinear complex nature of fluid dynamics is observed in nanometric length-scale, which is also one of the first studies in room temperature. Self-driven nanofluidics will have a large positive impact on biosensors, healthcare, net-zero sustainable energy production, and fundamental physics of fluid dynamics.

Structure: transpiration, evaporation, nanofluidics, Gibbs-Marangoni effect, anti-gravity flow.

INTRODUCTION

Nanometric cavities and pores are significantly useful for drag and heat transfer properties. Thus, the fundamental understanding of interfacial fluid dynamics of them is crucial to impact nanofluidic transport for molecular biology and sustainable energy. When two fluids of different densities contact each other, at the interface perturbations of molecular interactions create interference patterns, which is famously known as the Rayleigh-Taylor instabilities. The rate of development of these instabilities gives insights into the fluid dynamics of interfacial systems [1].

In this letter, we show self-driven flow dynamics through sub-100 nm nanofluidic pores. The reference velocity is estimated to that in the biological nanofluidic pores of leaf structures. Although nanofluidic pores have been a dynamic area of research over the past decades, biomimicking stable nanofluidic pore flow dynamics (less than 100 nm) will give rise to exceptional state-of-the-art engineering ideas at the nanoscale domain. Ability to control in growth mechanism is advantageous, like interfacial hydraulic resistance causes stomata to close in towering trees, which will change the approach in electronics and next generation propulsion [2].

Flow dynamics in nanofluidic pores remains unclear. The limitation not only lies in experimental difficulties but also in the theoretical aspects. We use the Rayleigh-Taylor instability model at the water-air interface is used to explain evaporation through nanofluidic pores similar to that present in a leaf surface. This can also explain the rate and extend of flow with the varying densities in a system of stable solid-state nanofluidic pores with no application of external voltage or pressure against gravity.

Nano channel transport mechanisms are always ought to be either voltage driven [3] or with a pressure gradient under the influence of gravity, but, our understanding of nature and its flow dynamics is still incomplete. In Figure 1a, the transport principle details that the flow direction diverges at the interface of the rigid wall, and the forces (van der Waals, electrostatic, induce dipole between polar and non-polar species, oscillatory solvation pressure) plays a huge role in the flow structure. The velocity through the nanofluidic pore changes with the position of the nanofluidic pore along the wall, even though the depth in the direction of gravity is unvaried. This variation is calculated for 30 nm, 50 nm, 70 nm single nanofluidic pore systems and plotted in Figure 1b. The flow through these nanofluidic pores is constrained in most cases due to some external factor like a high-pressure gradient.

MODEL DESCRIPTION OF NANOFUIDIC SYSTEMS

A nanofluidic liquid-gas interface for bulk-gas and bulk-water is depicted with unidirectional flow patterns obtained from our numerical simulation of the physical setup in Figure 1a. Such a system produces chaotic flow velocities and pressures at the nanofluidic interface if the position of the nanofluidic pores is varied from edge to the centre of the reservoir as shown in Figure 1b-c. To understand this system, we coupled the continuity, momentum, and energy equations for solving the Navier-Stokes equations describing the motion of viscous fluids. Since discretisation for structural analysis is efficient with the finite element method, we use it for simulating fluid flow in nanofluidic pore systems at the water-air interface in the view of the Rayleigh-Taylor instability model for fluids. We solve the flow equation and volume fraction equation. We consider volume fraction of water as 1 and

* Email of correspondence: sg915@cam.ac.uk

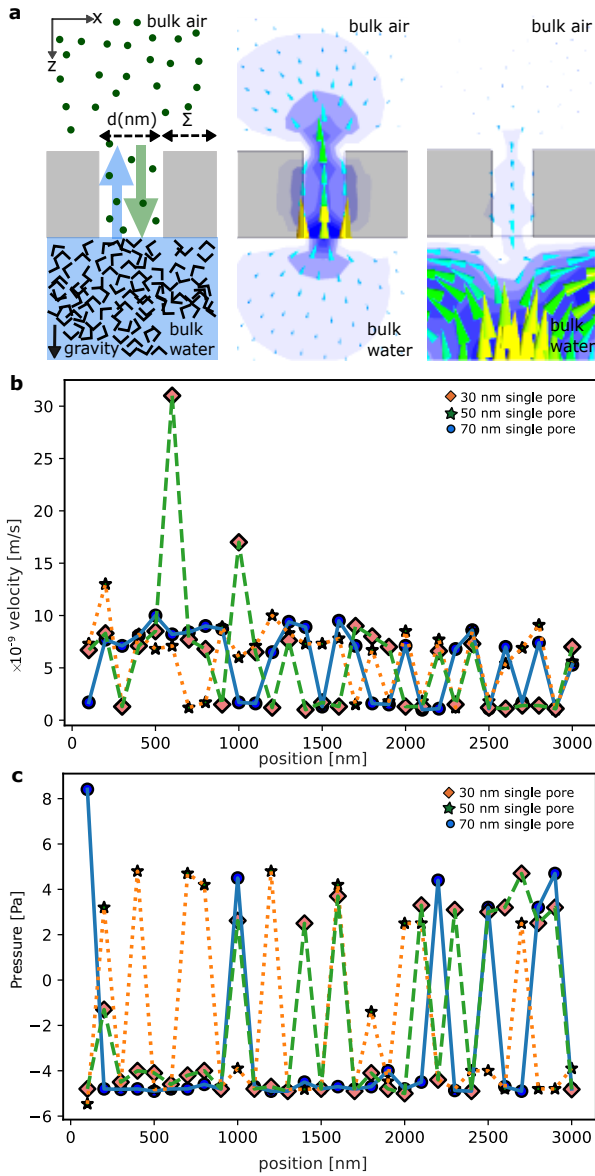


FIG. 1. **Liquid-gas interface nanofluidics.** (a) Principle of fluid flow at the interface of bulk air and bulk water in nanofluidic pore; Σ is the distance of nanofluidic pore from the RHS boundary, d (nm) is the nanofluidic pore throat diameter. (b) Variation of maximum velocity in mixture phase(at the interface) with d (nm) for 30 nm, 50 nm, and 70 nm single pore systems. (c) Dependence of pressure inside the nanofluidic pore with the distance from edge, Σ .

air as 0 for the Eulerian modelling of multiphase flow. The general fluid transport equation is given by,

$$\frac{\partial}{\partial t}(\alpha\rho\phi) + \nabla \cdot (\alpha\rho\mathbf{v}\phi) = \nabla \cdot \bar{\tau} + S\phi \quad (1)$$

where α is the phase volume fraction, ρ is the phase density, ϕ is the phase variable, \mathbf{v} is the phase velocity, S is the source term (added mass in the first phase dispersing to the other phase), and $\bar{\tau}$ is the diffusion term (stress tensor) [4]. This governs the flow of the system along

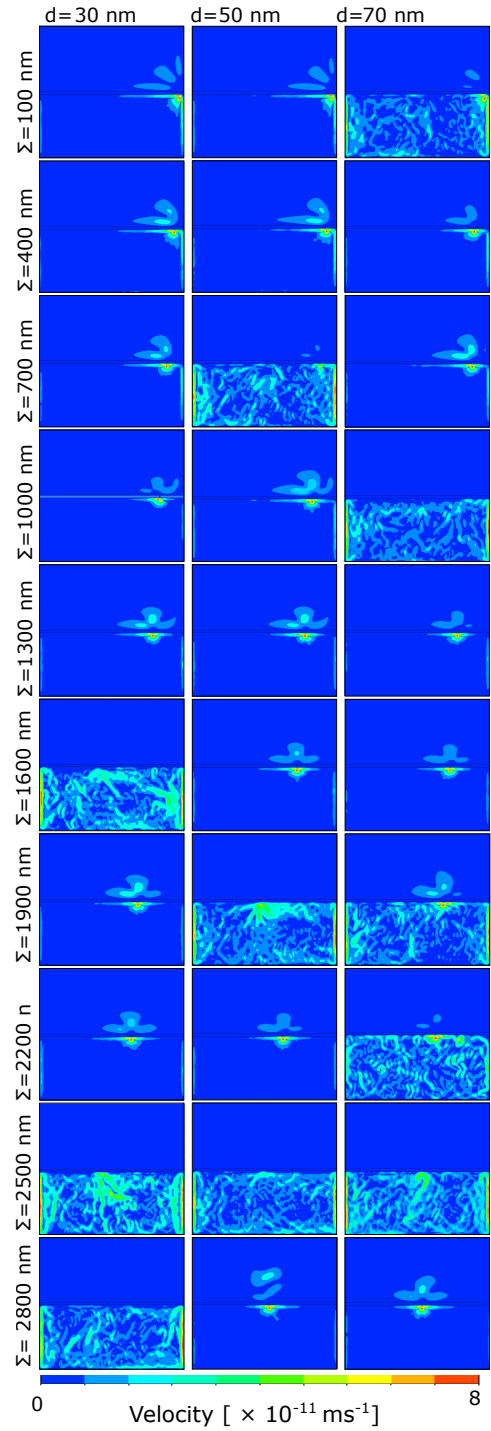


FIG. 2. Change in the velocity flow profile for 30 nm, 50 nm, and 70 nm nanofluidic pore systems with the distance from the edge, Σ .

with the volume fraction equation which is given by,

$$\frac{1}{\rho_q} \left[\frac{\partial}{\partial t}(\alpha_q\rho_q) + \nabla \cdot (\alpha_q\rho_q\mathbf{v}_q) \right] = S_{\alpha_q} + \sum_{p=1}^n (\dot{m}_{pq} - \dot{m}_{qp}) \quad (2)$$

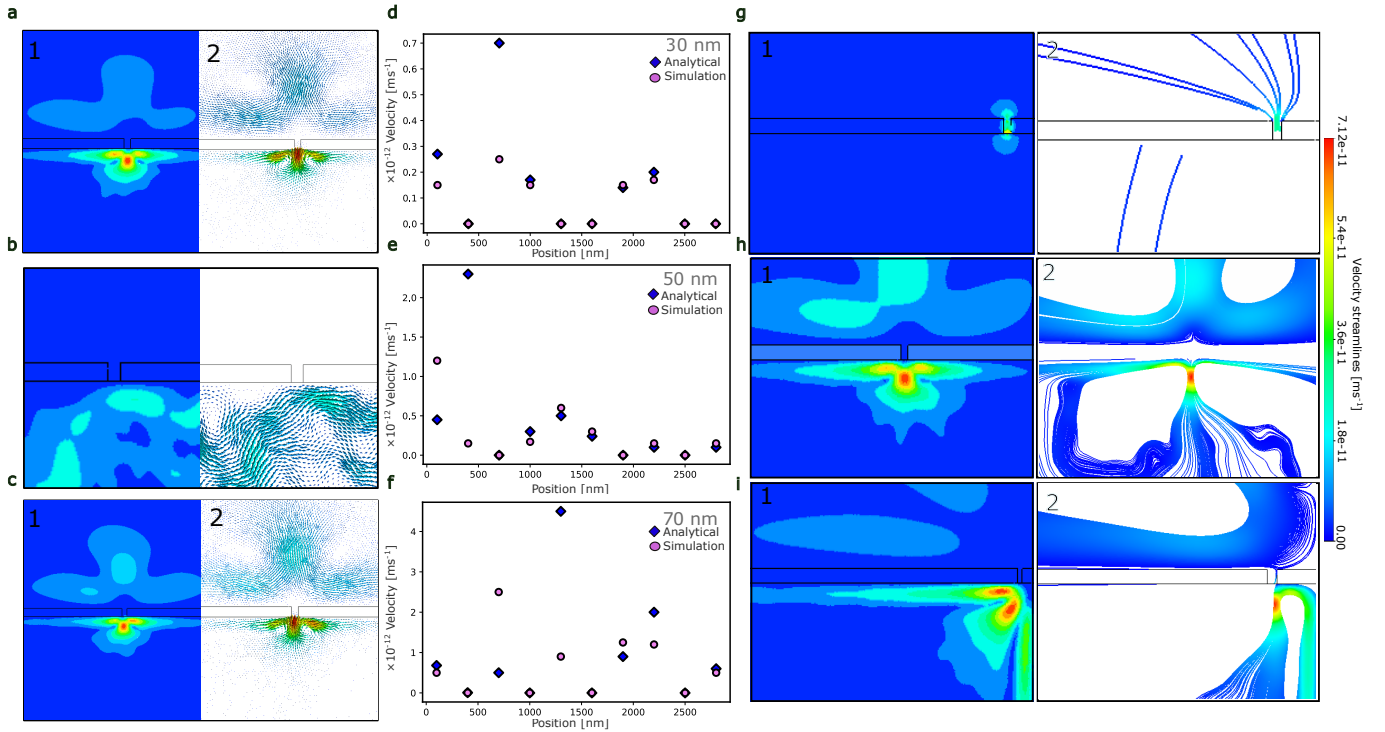


FIG. 3. (a) 70 nm single nanofluidic pore system at $\Sigma = 1700$ nm single nanofluidic pore system; 1 – velocity magnitude distribution in and 2 – velocity vectors indicating vertices in water and air resulting with no flow from water to air. (b) 70 nm single nanofluidic pore system at $\Sigma = 2200$ nm; 1 – velocity magnitude with high value near the opening and 2 – velocity vector with no flow in air but flow component. (c) 70 nm single nanofluidic pore system at $\Sigma = 1600$ nm; 1 – velocity magnitude and 2 – velocity vector with prominent back flow and vertices in water and air. (d) 30 nm, (e) 50 nm, and (f) 70 nm – Comparison of analytical and simulated velocity. (g) 30 nm, (h) 50 nm, and (i) 70 nm – Left: velocity magnitude distribution patterns and right: velocity streamlines.

where \dot{m}_{pq} is the mass transfer from phase p to phase q and \dot{m}_{qp} is the mass transfer from phase q to phase p [4]. This is dependant on the mass transfer through these nanofluidic pores regardless of the direction of flow. The difference in densities of the two fluids is expected to create a pressure gradient which results in fluid flow. A fluidic reservoir of $6000 \text{ nm} \times 6000 \text{ nm}$ is separated using a 100 nm wall. This separation at the water-air interface is constituted of 96% silicon wall with the physical properties of density $2.18 \times 10^{-12} \text{ g/m}^3$, elastic modulus $6.8 \times 10^{10} \text{ Pa}$, shear modulus $2.8 \times 10^{10} \text{ Pa}$, Poisson's ratio 0.19, thermal conductivity 1.38 W/mK , and specific heat $750 \text{ J/kg}^\circ\text{C}$. The multi-phase simulation considers specific heat for air and water to be 1006.43 J/kgK and 4182 J/kgK , respectively. We used a triangular mesh geometry with an average area of $9 \times 10^{-12} \text{ m}^2$ where element mesh size is $2.5 \times 10^{-8} \text{ m}$. The viscous model is set to laminar and implicit formulation was performed. The system temperature was set to 288.16 K . The area to length aspect ratio changes from case to case which is crucial in these systems. The fluid dynamics for single nanofluidic pore systems with a diameter (d) 30 nm, 50 nm, and 70 nm by varying the distance (Σ) from the boundary of the reservoir in the orthogonal direction of the gravity is shown in Figure 2. Until now, regardless of

the geometry, the interface between two fluids is considered to be linear. However, mesoscopic physics of fluidic interface is significantly complex in nanometric length scale, which is yet to be addressed. All simulations were performed in two dimensional and performed using ANSYS FLUENT 2021 R1 solver in Intel i7 CPU.

ANALYTICAL VALIDATION OF SELF-DRIVEN NANOFLUIDICS

We analytically validate the transport mechanism or flow structures as shown in Figure 2. We used densities of two fluids as $\rho_1 = 1.225 \text{ kg/m}^3$ (air) and $\rho_2 = 997 \text{ kg/m}^3$ (water). Since the domain is larger than the wavelength of the instabilities, the velocity potential of the motion is given by Taylor [1] as:

$$\phi_1 = Ae^{(-ky+nt)} \cos kx \quad (3)$$

$$\phi_2 = Ae^{(ky+nt)} \cos kx \quad (4)$$

where ϕ_1 is the velocity potential in air, A is the amplitude, k is the wave number, n is an integer, and ϕ_2 is the velocity potential in water. Assuming that acceleration

takes place towards the denser fluid. At the interface,

$$n^2 = -k(g_1 + g_2) \left(\frac{\rho_2 - \rho_1}{\rho_1 + \rho_2} \right) \quad (5)$$

For 30 nm single nanofluidic pore with maximum flow rate,

$$n^2 = -(2e - 11)kt. \quad (6)$$

For 50 nm single pore system with maximum flow rate,

$$n^2 = -(1.3e - 0.9)kt. \quad (7)$$

Since $(g_1 + g_2)$ is positive, the instability increases with time initially until it reaches a steady state after which it is proportional to $\sqrt{\frac{\rho_2 - \rho_1}{\rho_2 + \rho_1}}$, which is unity in our system and explains the no flow systems. For systems without flow Equation 2 is given by:

$$n^2 = 0 \quad (8)$$

The extend of the flow effect that penetrates inside the water phase is given by,

$$S = \frac{1}{2}g_1t^2 \quad (9)$$

where S is the displacement, time is calculated from initial time t (from 0 to t) after the steady state is achieved, g_1 is the acceleration of the molecular species, and v is the velocity of flow. In an evaporating liquid-gas interface, certain number of atoms/molecules condenses onto the surface of liquid. The ratio of atoms condensing to atoms evaporating is unclear and can be complicated to predict from system to system. The number of condensing molecules is a function of mean velocity through the nanofluidic pore. The number of evaporating particles is given by Feynman [5] in page 42-1 as $N = \frac{1}{\Gamma} \frac{\nu}{D} e^{(-W/k_B T)}$ where ν is the average speed of particle, W is the extra energy needed to get evaporates, k_B is the Boltzmann constant, and Γ is the cross-sectional area. Since we describe the system using continuum mechanics, we do not pursue this quantum mechanical perspective.

The vapour transport through nanofluidic pore is governed by the conventional Hagen-Poiseuille equation [6] which is given by

$$P_i - P_l = \frac{8\eta L \dot{m}}{\pi r^4 \rho_l} \quad (10)$$

where P_i is the pressure at the interface, P_l is the liquid phase pressure, m is the mass flow rate through the nanofluidic pore, η is the viscosity of the liquid, r is the radius of the nanofluidic pore, L is the flow length, and ρ is the liquid density. Since we are addressing transport in nanofluidic pores using the Rayleigh-Taylor instability:

$$\Delta P = \frac{4\eta g_1 t^2 \dot{m}}{\pi r^4 \rho_l} \quad (11)$$

$$\Delta P = \frac{8\eta \alpha_e n_e \dot{m}}{\pi r^4 \rho_l} \quad (12)$$

where α_e is the element size of the geometry used for simulation, n_e is the number of elements in the flow region, g_1 is the acceleration of the molecular species.

$$v = \frac{\Delta P \pi r^4 \rho_l t}{8\mu_l \dot{m}} \quad (13)$$

where v is the analytical velocity of the system, P is the pressure, t is the time and m is the mass flow rate. In the Rayleigh Taylor instability model, $S = 0.5gt^2$ is used in Equation 11 to find the velocity of the system.

In Figure 3d-f, we found strong agreement between analytical and numerical velocities except in few cases large errors are observed.

FLOW DYNAMICS IN SINGLE AND MULTIPLE NANOFLUIDIC PORES

The most common flow dynamics in all single nanofluidic pore systems is the cloud of spherical structure or hat shape with large flow velocities. The movement of the liquid along the nanofluidic pore to the air is hindered by a back-flow as in Figure 1c and the meniscus is visible in many cases in Figure 2. In Figure 2, we observe the sudden collapse of flow in the air region is found in certain positions of nanofluidic pores while varying the distance from 100 nm to 3000 nm. A driving mechanism that initiates and inhibits the flow is ubiquitous and continuous. The pressure drops above the meniscus induces a back-flow in the water to set it in motion as shown in several instances of 30 nm (at Σ 1600 nm, 2500 nm, and 2800 nm), 50 nm (at Σ 700 nm, 1900 nm, and 2500 nm), and 70 nm (at Σ 1000 nm, 1000 nm, 1900 nm, and 2500 nm). The distinct small peaks of velocity counter are observed on either side of the highest peak like that of the Gibbs-Marangoni flow [7] in Figure 2.

The maximum flow rate through 30 nm, 50 nm, 70 nm systems are found to be $1.3 \times 10^{-11} \text{ ms}^{-1}$, $1.3 \times 10^{-9} \text{ ms}^{-1}$, $8.4 \times 10^{-9} \text{ ms}^{-1}$, respectively when the reference flow velocity through the nanofluidic pore is set to be $4.2 \times 10^{-9} \text{ ms}^{-1}$. The disruption of equilibrium at the interface and the backflow through the nanofluidic pore to the water domain can cause the phenomenon of cavitation [8] which hinders the further flow which is not uncommon in transport through confined nanofluidic pore systems. Usually, the variations in contact angle and the liquid pressure at the interface control the evaporation process to a great extent and heat is to be supplied for it to sustain [6].

In Figure 3 and Figure 4, the velocity vectors show flow in both directions of water and air without applying any external driving force with a high probability of flow in the direction against the gravity from water to

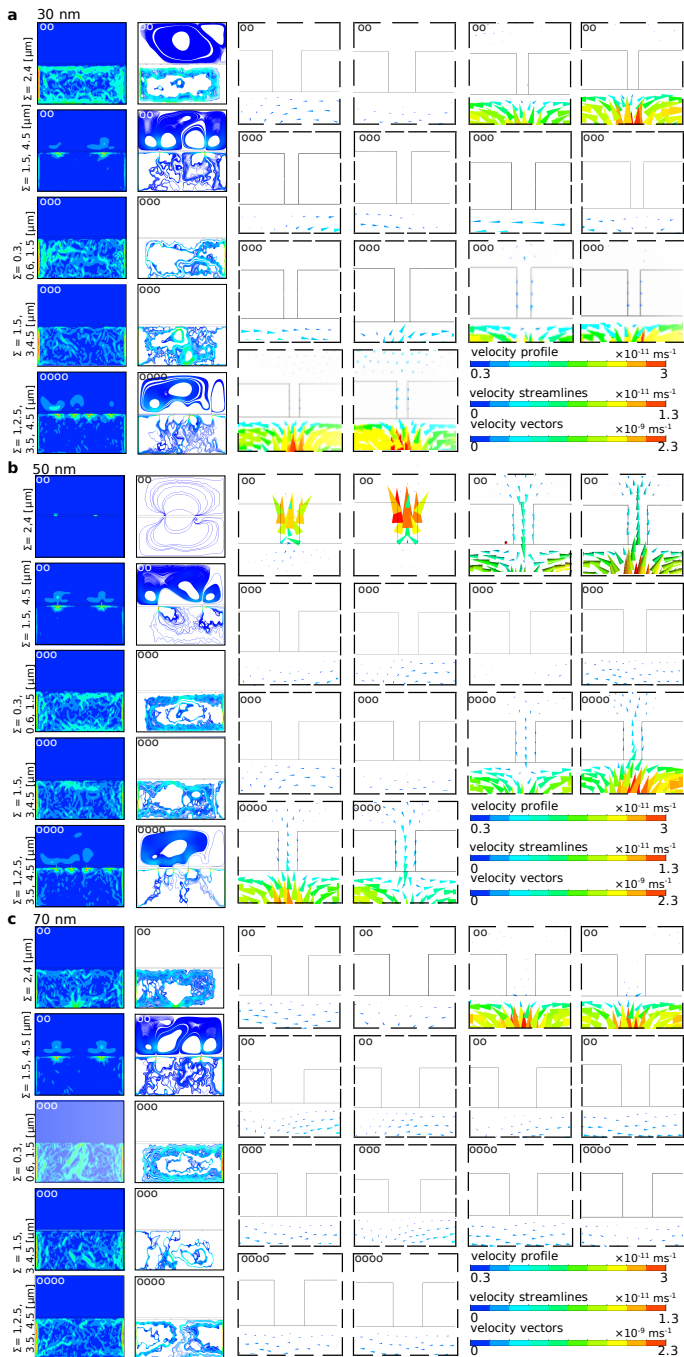


FIG. 4. Flow dynamics of multiple nanofluidic pore systems. Velocity flow profile and corresponding velocity stream lines and velocity vector for (a) 30 nm – two pores ‘oo’, three pores ‘ooo’, and four pores ‘oooo’, (b) 50 nm – two pores ‘oo’, three pores ‘ooo’, and four pores ‘oooo’, and (c) 70 nm – two pores ‘oo’, three pores ‘ooo’, and four pores ‘oooo’ by varying Σ or the distance between the pores and wall.

air. Figure 3a represents the systems where the cloud of high-velocity molecules exist and the velocity vectors are pointed towards the air volume fraction. Figure 3b represents the systems with no flow in the air and the

strong back-flow in water creates vertices throughout the boundaries. The velocity vectors show several asymmetric swirls and sudden changes in directions with a turbulent nature. In Figure 3c represent a system with a significant flow. Here, back-flow towards the water phase is initiated but is relatively less prominent than the velocity vectors towards the water phase (Figure 3c).

Now let us discuss the flow structures that are most likely to occur in a stable confined nanofluidic pore based on the velocity of molecular species in the system. Figure 3g-i and their variants are the most observed velocity distributions within all the single-pore systems. In Figure 4, the velocity distribution of the multiple nanofluidic pore system become more complex than the single nanofluidic pore system. This is indicative that the molecular species in the (NVT) ensemble distribute their kinetic energy in a way to maintain the number of evaporated molecules and the number of condensing molecules in equilibrium.

SUMMARY

Rayleigh Taylor-instability of water and air in sub-100 nanometer fluidic pores behave in a non-trivial manner. Large flow velocities in the range of nm/s can be created through nanofluidic pores without applying any external driving force. At the same time, flow can be turned off by turning the position of the nanofluidic pores from the wall or by introducing additional pores. We have developed a fundamental understanding of nanofluidic flow dynamics by studying diverse cases in the context of parameters, such as applied pressure, position to pore size ratio of the nanofluidic pore, gravity, and density. This first report of self-driven flow and its switching mechanism will open new avenues of scientific research of the highly nonlinear complex nature of fluid dynamics at the nanometre length scale. These complex nature can be due to the co-existence of components which do not follow the conventional viscosity which can eventually head further towards the concept of coupling of an-harmonic and harmonic components in the same system at room temperature. It will have a positive impact on net-zero sustainable energy production, nanorobotic manipulation, biomolecular diagnostics, and the fundamental physics of fluid dynamics.

AUTHORS’ CONTRIBUTION

VJ performed the simulation and analyses. SG developed the core idea and supervised the research. VJ and SG both have written the manuscript.

ACKNOWLEDGMENTS

The authors are grateful to the International Center for Nanodevices for funding. SG thanks the German Research Foundation for funding his research.

- [1] G. I. Taylor, The instability of liquid surfaces when accelerated in a direction perpendicular to their planes. i, Proceedings of the Royal Society of London. Series A. Mathematical and Physical Sciences **201**, 192 (1950).
- [2] B. J. Yoder, M. G. Ryan, R. H. Waring, A. W. Schoettle, and M. R. Kaufmann, Evidence of Reduced Photosynthetic Rates in Old Trees, Forest Science **40**, 513 (1994), <https://academic.oup.com/forestscience/article-pdf/40/3/513/22549777/forestscience0513.pdf>.
- [3] A. Meller and D. Branton, Single molecule measurements of dna transport through a nanopore, Electrophoresis **23**, 2583 (2002).
- [4] U. Manual, Ansys fluent 12.0, Theory Guide (2009).
- [5] R. P. Feynman, R. B. Leighton, and M. Sands, The feynman lectures on physics; vol. i, American Journal of Physics **33**, 750 (1965).
- [6] Z. Lu, S. Narayanan, and E. N. Wang, Modeling of evaporation from nanopores with nonequilibrium and nonlocal effects, Langmuir **31**, 9817 (2015).
- [7] S. Narayanan, A. G. Fedorov, and Y. K. Joshi, Interfacial transport of evaporating water confined in nanopores, Langmuir **27**, 10666 (2011).
- [8] J. S. Sperry, Evolution of water transport and xylem structure, International Journal of Plant Sciences **164**, S115 (2003).
- [9] G. Chen, C. Boothroyd, and C. Humphreys, Electron-beam-induced damage in amorphous sio2 and the direct fabrication of silicon nanostructures, Philosophical Magazine A **78**, 491 (1998).
- [10] S. Nekolla, C. Andersen, and R. Benz, Noise analysis of ion current through the open and the sugar-induced closed state of the lamb channel of escherichia coli outer membrane: evaluation of the sugar binding kinetics to the channel interior, Biophysical journal **66**, 1388 (1994).
- [11] C. Guo, J. Xu, K. Wu, M. Wei, and S. Liu, Study on gas flow through nano pores of shale gas reservoirs, Fuel **143**, 107 (2015).
- [12] W. Song, J. Yao, D. Wang, Y. Li, H. Sun, and Y. Yang, Dynamic pore network modelling of real gas transport in shale nanopore structure, Journal of Petroleum Science and Engineering **184**, 106506 (2020).
- [13] S. Roy, R. Raju, H. F. Chuang, B. A. Cruden, and M. Meyyappan, Modeling gas flow through microchannels and nanopores, Journal of applied physics **93**, 4870 (2003).
- [14] S. Howorka and Z. Siwy, Nanopore analytics: sensing of single molecules, Chemical Society Reviews **38**, 2360 (2009).
- [15] W. Liu, Y. Sun, H. Yan, Y. Ren, C. Song, and Q. Wu, A simulation analysis of nanofluidic ion current rectification using a metal-dielectric janus nanopore driven by induced-charge electrokinetic phenomena, Micromachines **11**, 542 (2020).
- [16] A. Zou, M. Gupta, and S. C. Maroo, Transpiration mechanism in confined nanopores, The journal of physical chemistry letters **11**, 3637 (2020).
- [17] V. Goncharov, Analytical model of nonlinear, single-mode, classical rayleigh-taylor instability at arbitrary atwood numbers, Physical review letters **88**, 134502 (2002).
- [18] Y. Li, H. Chen, S. Xiao, M. A. Alibakhshi, C.-W. Lo, M.-C. Lu, and C. Duan, Ultrafast diameter-dependent water evaporation from nanopores, Acs Nano **13**, 3363 (2019).
- [19] P. Jin, *Fabrication of synthetic nanopores in thin films for studies of analytical applications* (University of Florida, 2009).
- [20] L. T. Sexton, L. P. Horne, and C. R. Martin, Developing synthetic conical nanopores for biosensing applications, Molecular BioSystems **3**, 667 (2007).
- [21] C. Sternling, , and L. Scriven, Interfacial turbulence: hydrodynamic instability and the marangoni effect, AIChE Journal **5**, 514 (1959).
- [22] R. Liu and Z. Liu, Self-pumping ultra-thin film evaporation on cnt-embedded silicon nitride nanopore membrane, Nano Research , 1 (2021).
- [23] R. M. Smeets, U. Keyser, M. Wu, N. Dekker, and C. Dekker, Nanobubbles in solid-state nanopores, Physical Review Letters **97**, 088101 (2006).
- [24] M. Suk and N. Aluru, Molecular and continuum hydrodynamics in graphene nanopores, RSC advances **3**, 9365 (2013).

Appendix A: Governing differential equations

The Navier-Stokes equation holds the following governing equations to define a fluid motion. The continuity equation is given by:

$$\frac{\partial \rho}{\partial t} + \frac{\partial \rho u}{\partial x} + \frac{\partial \rho v}{\partial y} + \frac{\partial \rho w}{\partial z} = 0 \quad (\text{A1})$$

where (u, v, w) are the velocity components in (x, y, z) direction respectively, t is the time (usually a large time period is considered for steady state simulation), p is the pressure, and ρ is the density. The momentum equation in equation A1 is given by

x-component

$$\begin{aligned} \frac{\partial(\rho u)}{\partial t} + \frac{\partial(\rho u^2)}{\partial x} + \frac{\partial(\rho uv)}{\partial y} + \frac{\partial(\rho uw)}{\partial z} = \\ -\frac{\partial p}{\partial x} + \frac{1}{Re} \left[\frac{\partial \bar{\tau}_{xx}}{\partial x} + \frac{\partial \bar{\tau}_{xy}}{\partial y} + \frac{\partial \bar{\tau}_{xz}}{\partial z} \right] \end{aligned} \quad (\text{A2})$$

y-component

$$\begin{aligned} \frac{\partial(\rho v)}{\partial t} + \frac{\partial(\rho uv)}{\partial x} + \frac{\partial(\rho v^2)}{\partial y} + \frac{\partial(\rho vw)}{\partial z} = \\ -\frac{\partial p}{\partial y} + \frac{1}{Re} \left[\frac{\partial \bar{\tau}_{xy}}{\partial x} + \frac{\partial \bar{\tau}_{yy}}{\partial y} + \frac{\partial \bar{\tau}_{yz}}{\partial z} \right] \end{aligned} \quad (\text{A3})$$

z-component

$$\begin{aligned} \frac{\partial(\rho w)}{\partial t} + \frac{\partial(\rho uw)}{\partial x} + \frac{\partial(\rho vw)}{\partial y} + \frac{\partial(\rho w^2)}{\partial z} = \\ -\frac{\partial p}{\partial z} + \frac{1}{Re} \left[\frac{\partial \bar{\tau}_{xz}}{\partial x} + \frac{\partial \bar{\tau}_{yz}}{\partial y} + \frac{\partial \bar{\tau}_{zz}}{\partial z} \right] \end{aligned} \quad (\text{A4})$$

The energy is given by

$$\frac{\partial(\rho E)}{\partial t} + \nabla \cdot (\mathbf{v}(\rho E + p)) = \nabla \cdot (k_{eff} \Delta T) + S_h \quad (\text{A5})$$

where E energy and T temperature are mass-averaged variable according to the volume of fraction model, p is phase parameter, k_{eff} is the effective thermal conductivity, S_h is the term which has contribution from radiation [4].

Appendix B: Detailed flow velocity of single nanofluidic pore systems

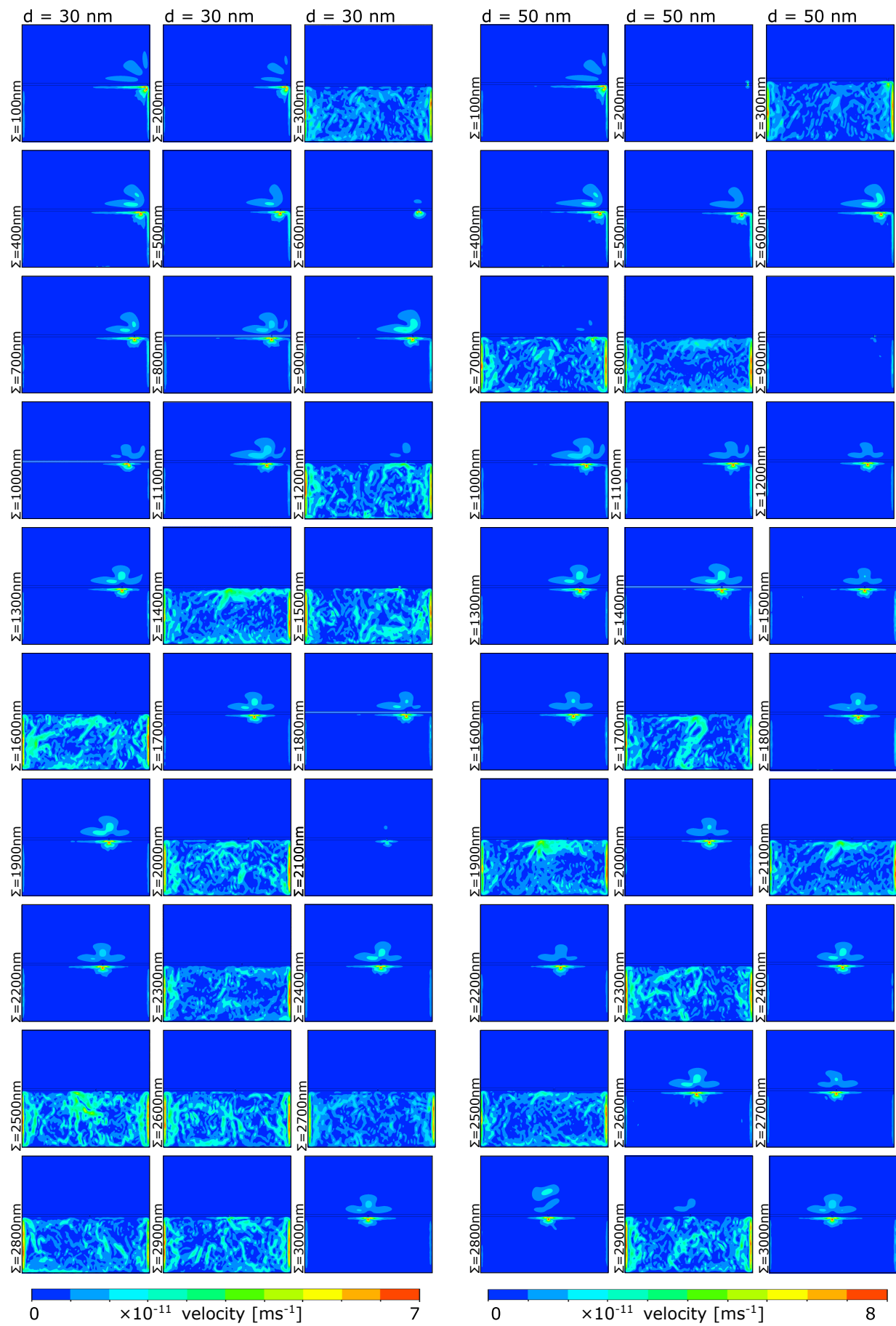


FIG. 5. Detailed flow dynamics of 30 nm and 50 nm single nanofluidic pore systems.

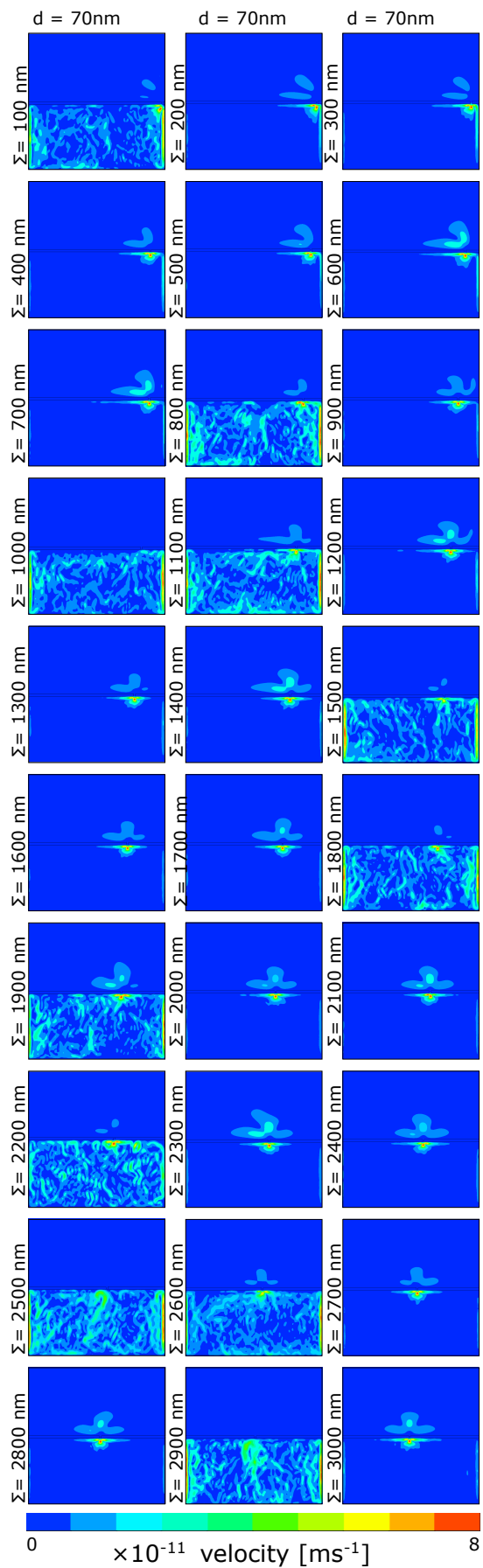


FIG. 6. Detailed flow dynamics of 70 nm single nanofluidic pore system.